

Deterministic multi-qubit entanglement in a quantum network

<https://doi.org/10.1038/s41586-021-03288-7>

Received: 11 September 2020

Accepted: 15 December 2020

Published online: 24 February 2021

 Check for updates

Youpeng Zhong^{1,4}, Hung-Shen Chang¹, Audrey Bienfait^{1,5}, Étienne Dumur^{1,2,6}, Ming-Han Chou^{1,3}, Christopher R. Conner¹, Joel Grebel¹, Rhys G. Povey^{1,3}, Haoxiong Yan¹, David I. Schuster^{1,3} & Andrew N. Cleland^{1,2}✉

The generation of high-fidelity distributed multi-qubit entanglement is a challenging task for large-scale quantum communication and computational networks^{1–4}. The deterministic entanglement of two remote qubits has recently been demonstrated with both photons^{5–10} and phonons¹¹. However, the deterministic generation and transmission of multi-qubit entanglement has not been demonstrated, primarily owing to limited state-transfer fidelities. Here we report a quantum network comprising two superconducting quantum nodes connected by a one-metre-long superconducting coaxial cable, where each node includes three interconnected qubits. By directly connecting the cable to one qubit in each node, we transfer quantum states between the nodes with a process fidelity of 0.911 ± 0.008 . We also prepare a three-qubit Greenberger–Horne–Zeilinger (GHZ) state^{12–14} in one node and deterministically transfer this state to the other node, with a transferred-state fidelity of 0.656 ± 0.014 . We further use this system to deterministically generate a globally distributed two-node, six-qubit GHZ state with a state fidelity of 0.722 ± 0.021 . The GHZ state fidelities are clearly above the threshold of $1/2$ for genuine multipartite entanglement¹⁵, showing that this architecture can be used to coherently link together multiple superconducting quantum processors, providing a modular approach for building large-scale quantum computers^{16,17}.

Superposition and entanglement are key resources that enable both quantum computing and quantum communication. The deterministic generation and distribution of entanglement in a scalable architecture is therefore a central requirement underpinning these technologies. Superconducting qubits show great promise as a scalable approach to building practical quantum computers^{18,19}, as well as for coherently linking superconducting processors within a cryostat^{5–8} or cryogenically linked cryostats²⁰. Developments in microwave-to-optical transduction promise further extensions of superconducting quantum networks^{21,22}, potentially allowing long-distance quantum communication^{23,24}. However, fundamental challenges still remain. In particular, the fidelity of chip-to-chip quantum state transfers using microwave-frequency photons has been limited to ~ 0.8 owing to losses in the communication channels^{5–8,20}, although experiments that minimize this loss point to the potential for high-fidelity communication^{9,25,26}. Here, we demonstrate a very low-loss connection between two physically distant quantum nodes fabricated on separate dies, with which we demonstrate a state-transfer fidelity of 0.911 ± 0.008 . This allows us to deterministically transfer fully entangled GHZ states between the two nodes, as well as generate a full two-node entangled state, paving the way for modular approaches to large-scale quantum computing and intra-cryostat quantum communication¹⁶.

Our quantum network consists of two nodes A and B, shown in Fig. 1, where each node is a superconducting processor comprising three capacitively coupled superconducting qubits Q_i^n ($i = 1, 2, 3$; $n = A, B$), with a tunable coupler²⁷ G^n connected to Q_2^n (see Supplementary Information for device fabrication details). We use a 1-m-long niobium–titanium (NbTi) superconducting coaxial cable to connect the two nodes together, with a time-variable coupling strength $g^n(t)$ controlled by the tunable coupler G^n in each node. To build a high-quality communication channel, we avoid use of microwave connectors or circulators^{5–8}, relying instead on direct superconducting aluminium wirebond connections between the coaxial cable and the processors; see Supplementary Information for more details.

We place the assembled quantum network in a magnetic shield attached to the mixing chamber of a dilution refrigerator with a base temperature below 10 mK (see Supplementary Information for experimental details). We first tune up and calibrate the quantum state transfer between Q_2^A and Q_2^B , with the other qubits biased far away in frequency. When the coupling is off, the coaxial cable is effectively shorted to ground on both ends, supporting an evenly spaced sequence of standing microwave modes, with a free spectral range of $\omega_{\text{FSR}}/(2\pi) = 105$ MHz. The coupling strength g^n between Q_2^n and each mode is determined by the superconducting phase δ^n across the Josephson junction of coupler G^n (see Supplementary Information for tunable coupler details). To tune up each qubit, we isolate the qubits from the cable by

¹Pritzker School of Molecular Engineering, University of Chicago, Chicago, IL, USA. ²Institute for Molecular Engineering and Material Science Division, Argonne National Laboratory, Argonne, IL, USA. ³Department of Physics, University of Chicago, Chicago, IL, USA. ⁴Present address: Shenzhen Institute for Quantum Science and Engineering, Southern University of Science and Technology, Shenzhen, China. ⁵Present address: Université de Lyon, ENS de Lyon, Université Claude Bernard, CNRS, Laboratoire de Physique, Lyon, France. ⁶Present address: Université Grenoble Alpes, CEA, INAC-Phelqs, Grenoble, France. ✉e-mail: anc@uchicago.edu

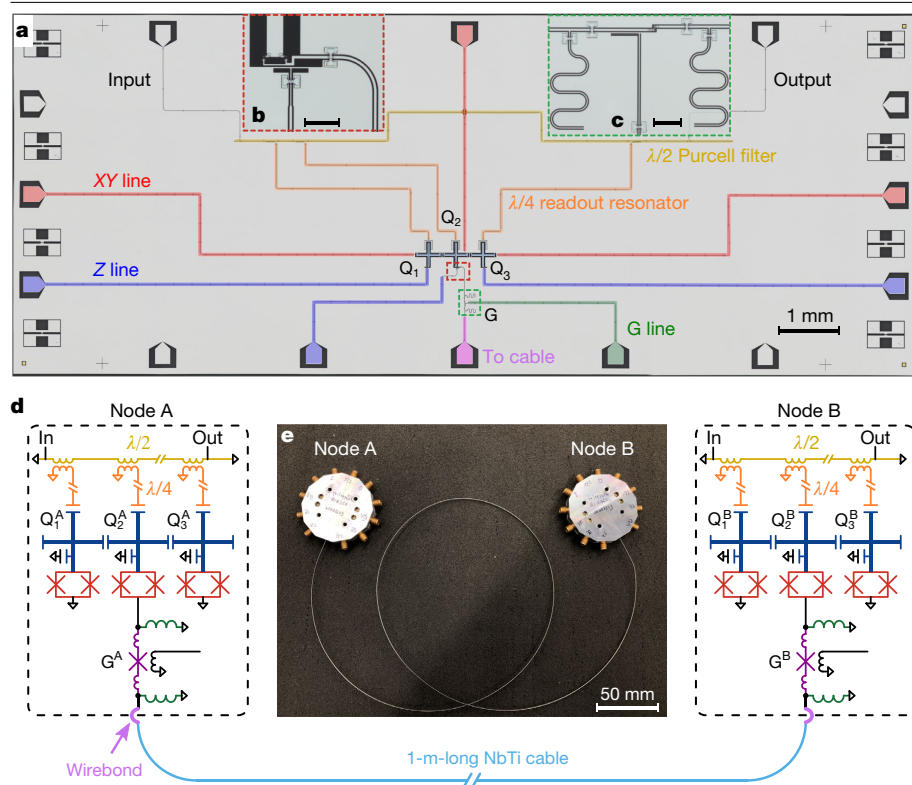


Fig. 1 | Device description. **a**, False-colour micrograph of one quantum processor node consisting of three capacitively coupled superconducting qubits Q_i ($i=1, 2, 3$) with a tunable coupler G connected to Q_2 . **b, c**, Higher-magnification micrographs of the Q_2 Josephson junctions (**b**) and the tunable coupler G (**c**). Scale bars are $50\ \mu\text{m}$. **d**, Schematic of the quantum network, consisting of two nodes A and B connected by a 1-m-long superconducting NbTi coaxial cable. Each node is a quantum processor of the type shown in panel **a**. **e**, Photograph of the quantum network assembly, where each node is in a machined-aluminium sample holder connected internally to the superconducting cable.

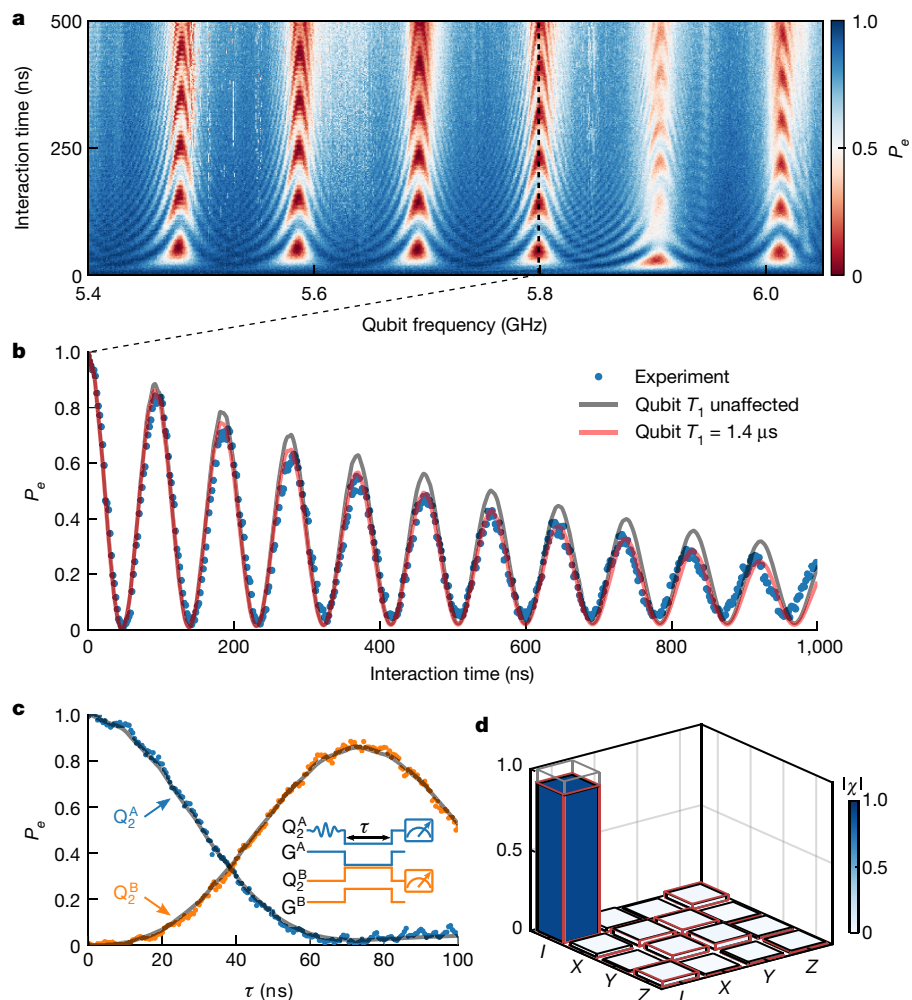


Fig. 2 | Quantum state transfer between node A and node B. **a**, Vacuum Rabi oscillations between Q_2^A and six standing modes in the coaxial cable, with coupling strength $g^A/(2\pi) \approx 5.5\ \text{MHz}$. **b**, Slice through the data in **a**, showing the vacuum Rabi oscillation of Q_2^A with the communication mode R at $5.798\ \text{GHz}$. Numerical simulations suggest that the effective qubit lifetime T_1 is shortened to $1.4\ \mu\text{s}$ during the interaction owing to loss associated with the cable connections; see Supplementary Information for details. **c**, Quantum state transfer from node A to node B using a hybrid transfer scheme, where Q_2^A and Q_2^B are resonantly coupled to R with the same coupling strength $g_r/(2\pi) = 4\ \text{MHz}$ for a duration τ . At $\tau = 72\ \text{ns}$, we achieve a single-photon transfer efficiency of $\eta = 0.881 \pm 0.008$. Grey lines denote numerical simulations. The inset shows the control pulse sequence. **d**, Process matrix χ for the quantum state transfer, corresponding to a process fidelity $\mathcal{F}^{\mathcal{P}} = 0.911 \pm 0.008$. The solid bars and red and grey frames are the measured, simulated and ideal values, respectively. The horizontal axes show the Pauli operators, I, X, Y, Z .

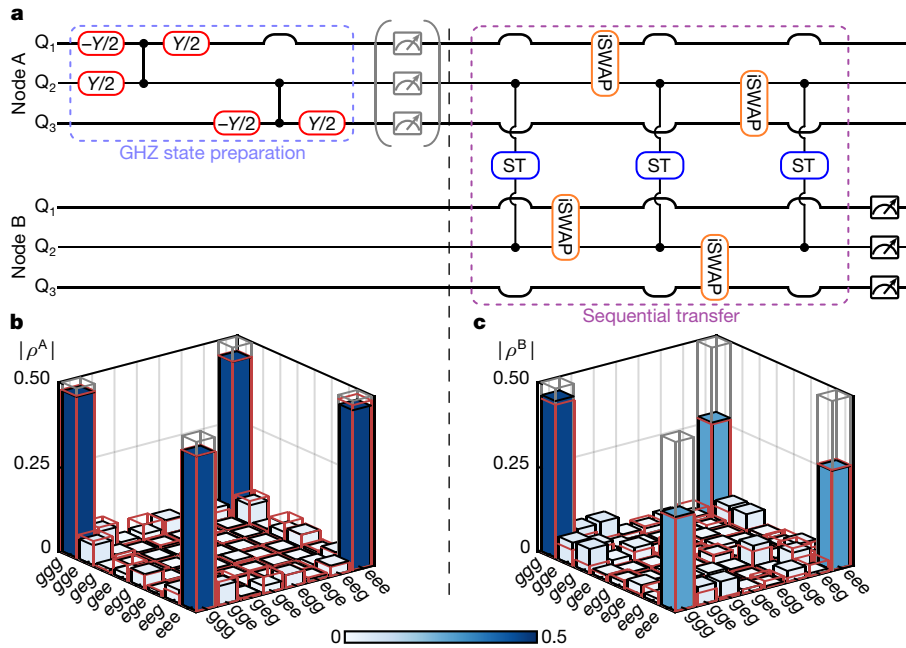


Fig. 3 | Deterministic transfer of a three-qubit GHZ state. a, Schematic of the GHZ state preparation and the sequential state-transfer (ST) protocol. Bumps in the horizontal lines are detuning pulses applied to Q_j^n ($j=1, 3$) to minimize interactions between these qubits and Q_2^n during the state-transfer and CZ operations. Measurement of the qubits in node A is only done to characterize

the prepared GHZ state, and is not performed when transferring the state to node B. **b**, Density matrix ρ^A of the GHZ state prepared in node A with a state fidelity of 0.931 ± 0.012 . **c**, Density matrix ρ^B of the state received in node B with a state fidelity of 0.656 ± 0.014 . Solid bars and red and grey frames are measured, simulated and ideal values, respectively.

biasing the coupler junction to $\delta^n = \pi/2$, turning off the coupling, $g^n \approx 0$. We find that each qubit has an intrinsic lifetime of $T_1 \approx 10 \mu\text{s}$ and a dephasing time of $T_\phi \approx 3 \mu\text{s}$; see Supplementary Table 1 for details.

When we prepare qubit Q_2^A in its excited state $|e\rangle$ and subsequently turn on coupler G^A to $g^A/(2\pi) \approx 5.5 \text{ MHz}$, we observe a sequence of vacuum Rabi oscillations between Q_2^A and the cable standing modes as we vary the qubit frequency and the interaction time, shown in Fig. 2a, where P_e is the probability of measuring the qubit in state $|e\rangle$. Because the mode at 5.798 GHz (dashed line) has a slightly longer lifetime ($T_{1r} = 473 \text{ ns}$) than the other modes, we use this as the communication mode R. The on-resonant vacuum Rabi oscillation between Q_2^A and R is shown in detail in Fig. 2b; more details are provided in Supplementary Information.

If both qubits Q_2^A and Q_2^B are resonantly coupled to R, the tripartite system has a ‘dark’ and two ‘bright’ eigenmodes, with very little occupation of the cable in the dark eigenmode²⁵. As proposed in ref.²⁸ and demonstrated in refs.^{8,25}, high-fidelity quantum state transfers can be achieved using the dark eigenmode even in the presence of considerable cable loss, albeit with limited transfer rates. Because we have both cable and qubit loss, we implement a hybrid state-transfer scheme²⁸, which involves all three eigenmodes in a way that balances these different losses. The hybrid scheme involves setting both G^A and G^B to the same coupling strength of $g_0/(2\pi) = 4 \text{ MHz}$ while tuning both Q_2^A and Q_2^B to be resonant with R for a duration of τ , shown in Fig. 2c. At $\tau = 72 \text{ ns}$, one photon is transferred from node A to node B with an efficiency of $\eta = 0.881 \pm 0.008$ (all reported uncertainties represent the standard deviation of repeated measurements); numerical simulations including the measured loss are in excellent agreement with the measurements (see Supplementary Information for simulation details). We perform quantum process tomography to characterize this state-transfer process, yielding the process matrix χ shown in Fig. 2d, with a process fidelity of $\mathcal{F}^p = \text{tr}(\chi\chi_{\text{ideal}}) = 0.911 \pm 0.008$, where χ_{ideal} is the process matrix for the identity operation \mathbb{I} . Numerical simulations give a process fidelity of 0.920. These simulations imply that the state-transfer process could be further improved by reducing loss associated with the cable and its interconnects.

In addition to the single-qubit state-transfer process, we tune up controlled-NOT (CNOT) gates built from controlled-Z (CZ) gates combined with single-qubit $\pi/2$ rotations, as well as tuning up iSWAP gates. The iSWAP gate is implemented by biasing Q_j^n ($j=1, 3$) to be resonant with Q_2^n for a duration of $\tau_{\text{swap}} = \pi/(2g_{j,2}^n) \approx 15 \text{ ns}$, where $g_{j,2}^n/(2\pi) \approx 16.7 \text{ MHz}$ is the capacitive coupling strength between Q_j^n and Q_2^n ; the iSWAP gate has a transfer efficiency of 0.99. The CZ gate is implemented²⁹ by biasing Q_2^n to be resonant with the $|e\rangle - |f\rangle$ transition frequency of $|e\rangle$ for a duration of $\tau_{\text{CZ}} = \pi/(\sqrt{2}g_{j,2}^n) \approx 21 \text{ ns}$, completing an $|ee\rangle \rightarrow -i|gf\rangle \rightarrow -|ee\rangle$ process that acquires an overall phase of π for the $|ee\rangle$ state, leaving the other basis states unchanged; here $|g\rangle$ and $|f\rangle$ are the ground state and the second excited state of the qubit, respectively. We characterize the CZ gate using quantum process tomography, obtaining a process matrix χ_{CZ} with an average process fidelity of 0.950 ± 0.006 (see Supplementary Information for more details about the iSWAP and CZ gates).

We use these gates to deterministically generate a GHZ state^{12–14} in node A, $|\psi_{\text{GHZ}}\rangle = (|ggg\rangle + |eee\rangle)/\sqrt{2}$ (written as $|Q_1^A Q_2^A Q_3^A\rangle$), which we then transfer to node B using the protocol shown in Fig. 3a. This involves two CNOT gates to prepare the state, followed by three sequential state transfers through the cable using Q_2^n ($n=A, B$), interleaved with iSWAPs with Q_1^n or Q_3^n .

The density matrix ρ^A of the three-qubit GHZ state in node A is measured using quantum state tomography and shown in Fig. 3b, with a state fidelity of $\mathcal{F}^A = \langle \psi_{\text{GHZ}} | \rho^A | \psi_{\text{GHZ}} \rangle = 0.931 \pm 0.012$. Calculations using χ_{CZ} give a state fidelity of 0.938, in good agreement with the experiment. This state is then transferred to node B using three sequential state transfers with interleaved iSWAP gates, yielding the final state ρ^B in node B, as shown in Fig. 3c, with a GHZ state fidelity $\mathcal{F}^B = 0.656 \pm 0.014$, clearly above the threshold of $1/2$ for genuine multipartite entanglement¹⁵. A calculation applying $\chi^{\otimes 3}$ and the expected decoherence process to ρ^A gives a state fidelity of 0.648, agreeing well with the experiment.

Finally, we demonstrate the step-by-step generation of a six-qubit entangled state distributed in the network, using the protocol shown

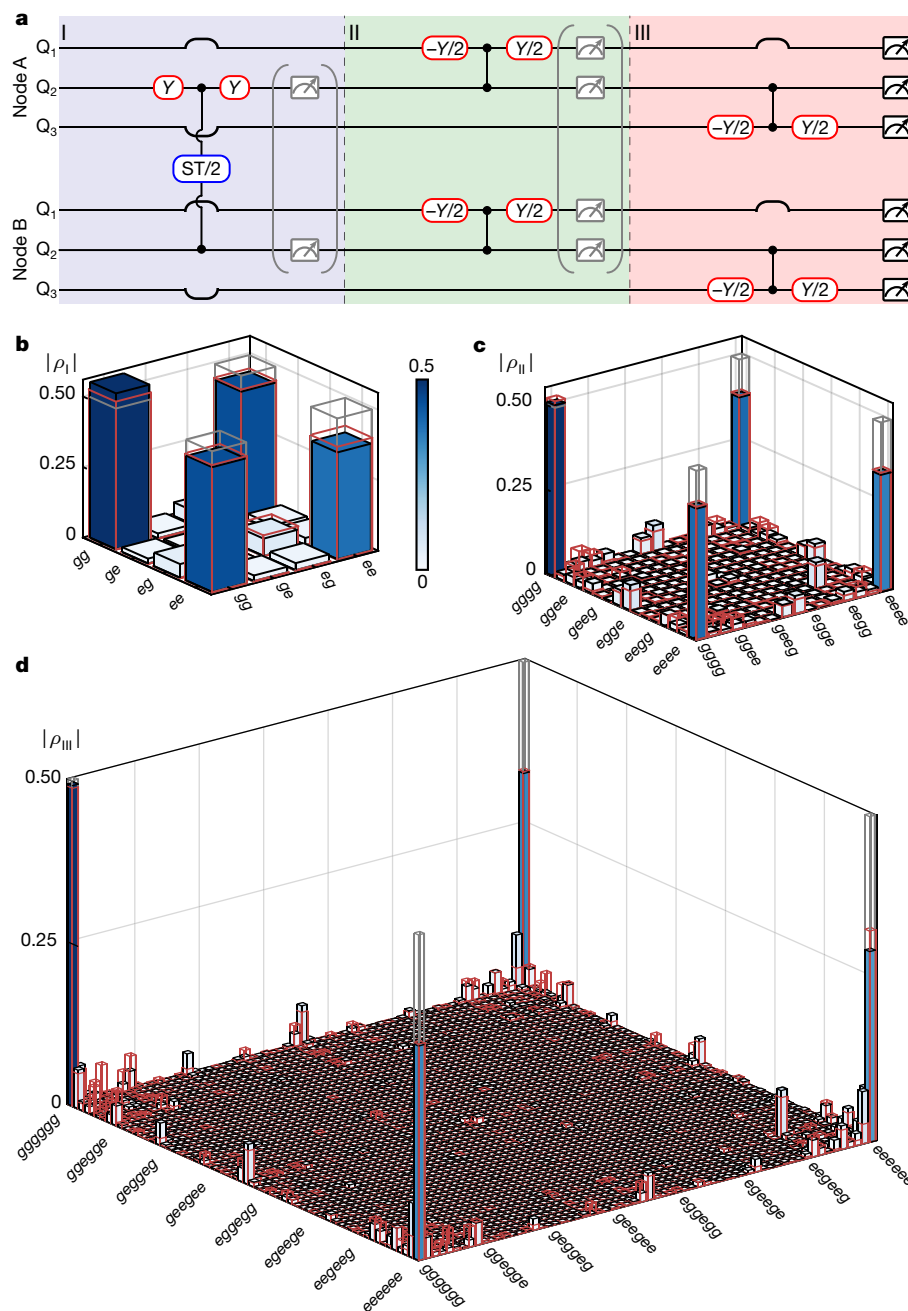


Fig. 4 | Deterministic generation of multi-qubit entanglement in a quantum network. **a**, The step-by-step protocol for entangling the two nodes, A and B. Here the ST/2 process involves transmitting half a photon from Q_2^A to Q_2^B . Bumps in the horizontal lines are detuning pulses. **b**, The Bell triplet state between Q_2^A and Q_2^B created in step I, with a state fidelity of 0.908 ± 0.012 . **c**, The

four-qubit GHZ state created in step II, with a state fidelity of 0.814 ± 0.008 . **d**, The six-qubit GHZ state created in step III, with a state fidelity of 0.722 ± 0.021 . The solid bars and red and grey frames are the measured, simulated and ideal values, respectively.

in Fig. 4a. In step I, we prepare a Bell triplet state $|B^+\rangle = (|gg\rangle + |ee\rangle)/\sqrt{2}$ (written as $|Q_2^A Q_2^B\rangle$), using an ST/2 process—similar to the state-transfer process, except the qubit frequencies and coupling parameters are adjusted so that an optimal Bell state fidelity is achieved at $\tau = 62.8$ ns (see Supplementary Information for details regarding the ST/2 process). The density matrix ρ_I for this process is shown in Fig. 4b, with a state fidelity of 0.908 ± 0.012 . Numerical simulations (see Supplementary Information) yield a state fidelity of 0.915. In step II, we apply CNOT gates between Q_1^A and Q_2^A to transform the Bell state into a four-qubit GHZ state $(|gggg\rangle + |eeee\rangle)/\sqrt{2}$ (written as $|Q_1^A Q_2^A Q_1^B Q_2^B\rangle$), with a density matrix ρ_{II} displayed in Fig. 4c with state fidelity 0.814 ± 0.008 . We finally

apply CNOT gates between Q_2^A and Q_3^A , creating a six-qubit GHZ state $(|gggggg\rangle + |eeeeee\rangle)/\sqrt{2}$ (written as $|Q_1^A Q_2^A Q_3^A Q_1^B Q_2^B Q_3^B\rangle$). The density matrix ρ_{III} of the entangled state is shown in Fig. 4d, with a state fidelity of 0.722 ± 0.021 , clearly above the threshold of 1/2 for genuine multipartite entanglement¹⁵. Numerical calculations (see Supplementary Information) give ρ_{II} and ρ_{III} with state fidelities of 0.829 and 0.738, respectively, agreeing well with the experiment.

In conclusion, we have built a two-node quantum network consisting of two three-qubit superconducting processor nodes connected by a 1-m-long superconducting coaxial cable. Using this system, we achieve a state-transfer process fidelity of 0.911 ± 0.008 between the

two nodes, which supports the deterministic generation and transfer of multi-qubit GHZ states. The transfer fidelity here is primarily limited by loss in the cable connections; improving these connections should yield considerable increases in the channel coherence and transfer fidelities. This architecture can be extended to coherently link more than two processor nodes, providing a modular solution for building large-scale quantum computers^{16,17}.

Online content

Any methods, additional references, Nature Research reporting summaries, source data, extended data, supplementary information, acknowledgements, peer review information; details of author contributions and competing interests; and statements of data and code availability are available at <https://doi.org/10.1038/s41586-021-03288-7>.

1. Nielsen, M. A. & Chuang, I. L. *Quantum Computation and Quantum Information* 2nd edn (Cambridge Univ. Press, 2010).
2. Gottesman, D. & Chuang, I. L. Demonstrating the viability of universal quantum computation using teleportation and single-qubit operations. *Nature* **402**, 390–393 (1999).
3. Duan, L.-M., Lukin, M. D., Cirac, J. I. & Zoller, P. Long-distance quantum communication with atomic ensembles and linear optics. *Nature* **414**, 413–418 (2001).
4. Jiang, L., Taylor, J. M., Sørensen, A. S. & Lukin, M. D. Distributed quantum computation based on small quantum registers. *Phys. Rev. A* **76**, 062323 (2007).
5. Kurpiers, P. et al. Deterministic quantum state transfer and remote entanglement using microwave photons. *Nature* **558**, 264–267 (2018).
6. Axline, C. J. et al. On-demand quantum state transfer and entanglement between remote microwave cavity memories. *Nat. Phys.* **14**, 705–710 (2018).
7. Campagne-Ibarcq, P. et al. Deterministic remote entanglement of superconducting circuits through microwave two-photon transitions. *Phys. Rev. Lett.* **120**, 200501 (2018).
8. Leung, N. et al. Deterministic bidirectional communication and remote entanglement generation between superconducting qubits. *npj Quantum Inf.* **5**, 18 (2019).
9. Zhong, Y. P. et al. Violating Bell's inequality with remotely connected superconducting qubits. *Nat. Phys.* **15**, 741–744 (2019).
10. Humphreys, P. C. et al. Deterministic delivery of remote entanglement on a quantum network. *Nature* **558**, 268–273 (2018); publisher correction **562**, E2 (2018).
11. Bienfait, A. et al. Phonon-mediated quantum state transfer and remote qubit entanglement. *Science* **364**, 368–371 (2019).
12. Greenberger, D. M., Horne, M. A., Shimony, A. & Zeilinger, A. Bell's theorem without inequalities. *Am. J. Phys.* **58**, 1131–1143 (1990).
13. Neeley, M. et al. Generation of three-qubit entangled states using superconducting phase qubits. *Nature* **467**, 570–573 (2010).
14. DiCarlo, L. et al. Preparation and measurement of three-qubit entanglement in a superconducting circuit. *Nature* **467**, 574–578 (2010).
15. Gühne, O. & Seevinck, M. Separability criteria for genuine multiparticle entanglement. *New J. Phys.* **12**, 053002 (2010).
16. Monroe, C. et al. Large-scale modular quantum-computer architecture with atomic memory and photonic interconnects. *Phys. Rev. A* **89**, 022317 (2014).
17. Chou, K. S. et al. Deterministic teleportation of a quantum gate between two logical qubits. *Nature* **561**, 368–373 (2018).
18. Arute, F. et al. Quantum supremacy using a programmable superconducting processor. *Nature* **574**, 505–510 (2019).
19. Rosenberg, D. et al. Solid-state qubits: 3D integration and packaging. *IEEE Microw. Mag.* **21**, 72–85 (2020).
20. Magnard, P. et al. Microwave quantum link between superconducting circuits housed in spatially separated cryogenic systems. *Phys. Rev. Lett.* **125**, 260502 (2020).
21. Bochmann, J., Vainsencher, A., Awschalom, D. D. & Cleland, A. N. Nanomechanical coupling between microwave and optical photons. *Nat. Phys.* **9**, 712–716 (2013).
22. Mirhosseini, M., Sipahigil, A., Kalaee, M. & Painter, O. Superconducting qubit to optical photon transduction. *Nature* **588**, 599–603 (2020).
23. Hensen, B. et al. Loophole-free Bell inequality violation using electron spins separated by 1.3 kilometres. *Nature* **526**, 682–686 (2015).
24. Liao, S.-K. et al. Satellite-to-ground quantum key distribution. *Nature* **549**, 43–47 (2017).
25. Chang, H.-S. et al. Remote entanglement via adiabatic passage using a tunably-dissipative quantum communication system. *Phys. Rev. Lett.* **124**, 240502 (2020).
26. Burkhardt, L. D. et al. Error-detected state transfer and entanglement in a superconducting quantum network. Preprint at <https://arxiv.org/abs/2004.06168> (2020).
27. Chen, Y. et al. Qubit architecture with high coherence and fast tunable coupling. *Phys. Rev. Lett.* **113**, 220502 (2014).
28. Wang, Y.-D. & Clerk, A. A. Using dark modes for high-fidelity optomechanical quantum state transfer. *New J. Phys.* **14**, 105010 (2012).
29. Strauch, F. W. et al. Quantum logic gates for coupled superconducting phase qubits. *Phys. Rev. Lett.* **91**, 167005 (2003).

Publisher's note Springer Nature remains neutral with regard to jurisdictional claims in published maps and institutional affiliations.

© The Author(s), under exclusive licence to Springer Nature Limited 2021

Methods

Quantum state-transfer and remote-entanglement protocols

Probabilistic remote entanglement has been realized with atomic ensembles^{30,31}, single atoms^{32,33}, defects in diamond^{23,34,35} and superconducting qubits^{36–39}. The deterministic entanglement of two remote qubits has recently been demonstrated with microwave photons^{5–9}, optical photons¹⁰ and surface acoustic wave phonons¹¹. For short-distance communication—for example, with microwave cables shorter than a few metres—the free spectral range of the cable is large enough that a single standing mode can relay quantum states^{9,40,41}, or state transfers can be via a ‘dark’ mode hybridized by a standing mode and the on-chip elements (qubits or resonators)^{8,25}. Here, we use a hybrid scheme²⁸ for state transfer, which balances the loss in the channel with that in the qubits, which might be further improved by optimizing the transfer process using shortcut-to-adiabatic-passage protocols^{42,43}.

If the length of the cable is increased, the free spectral range of the standing modes in the cable becomes smaller, making single-mode quantum state transfers more challenging. For long-distance communication, the use of itinerant photons is preferable^{44–46} but challenging in practice. Using tunable couplers to shape the photon emission and capture in a time-reversal symmetric manner, high-fidelity quantum state transfers have been achieved with itinerant photons^{5–7,47–51}; proposals using chiral communication channels point to the potential for quantum state transfers over thermal microwave networks^{52,53}. As demonstrated in earlier work⁹, the communication architecture here can also use itinerant photons to perform high-fidelity quantum state transfers.

Quantum state and process tomography

The density matrices of the Bell state and the GHZ states are characterized using quantum state tomography⁵⁴. After the state preparation and transfer, gates from the set $\{I, X/2, Y/2\}$ are applied to each qubit before the simultaneous readout of all qubits; the measured probabilities are corrected for readout errors, and the density matrix is reconstructed numerically. We use CVX, a Matlab package for specifying and solving convex programs, to reconstruct the density matrix while constraining it to be Hermitian, to have a unit trace and to be positive semidefinite. The single-shot simultaneous readout of the qubits is repeated 3×10^3 times to obtain the measured probabilities; the state tomography is run repeatedly, and in each repeat we reconstruct the density matrix and obtain the state fidelity. The fidelities and uncertainties of the quantum states correspond to the mean and standard deviation of 100 repeated measurements.

Quantum process tomography⁵⁵ for the state transfer is carried out by preparing Q_2^A in the input states $\{|g\rangle, (|g\rangle - |e\rangle)/\sqrt{2}, (|g\rangle + |e\rangle)/\sqrt{2}, |e\rangle\}$, then performing the quantum state-transfer process. The corresponding outcome density matrix in Q_2^B is measured using quantum state tomography as described above. The process matrix is reconstructed using the input and outcome density matrices, and using the CVX package to constrain it to be Hermitian, unit trace and positive semidefinite.

Data availability

The data that support the plots within this paper and other findings of this study are available from the corresponding author upon reasonable request.

30. Julsgaard, B., Kozhekin, A. & Polzik, E. S. Experimental long-lived entanglement of two macroscopic objects. *Nature* **413**, 400–403 (2001).

31. Chou, C.-W. et al. Measurement-induced entanglement for excitation stored in remote atomic ensembles. *Nature* **438**, 828–832 (2005).
32. Moehring, D. L. et al. Entanglement of single-atom quantum bits at a distance. *Nature* **449**, 68–71 (2007).
33. Ritter, S. et al. An elementary quantum network of single atoms in optical cavities. *Nature* **484**, 195–200 (2012).
34. Lee, K. C. et al. Entangling macroscopic diamonds at room temperature. *Science* **334**, 1253–1256 (2011).
35. Bernien, H. et al. Heralded entanglement between solid-state qubits separated by three metres. *Nature* **497**, 86–90 (2013).
36. Roch, N. et al. Observation of measurement-induced entanglement and quantum trajectories of remote superconducting qubits. *Phys. Rev. Lett.* **112**, 170501 (2014).
37. Narla, A. et al. Robust concurrent remote entanglement between two superconducting qubits. *Phys. Rev. X* **6**, 031036 (2016).
38. Dickel, C. et al. Chip-to-chip entanglement of transmon qubits using engineered measurement fields. *Phys. Rev. B* **97**, 064508 (2018).
39. Kurpiers, P. et al. Quantum communication with time-bin encoded microwave photons. *Phys. Rev. Appl.* **12**, 044067 (2019).
40. Sillanpää, M. A., Park, J. I. & Simmonds, R. W. Coherent quantum state storage and transfer between two phase qubits via a resonant cavity. *Nature* **449**, 438–442 (2007).
41. Majer, J. et al. Coupling superconducting qubits via a cavity bus. *Nature* **449**, 443–447 (2007).
42. Baksic, A., Ribeiro, H. & Clerk, A. A. Speeding up adiabatic quantum state transfer by using dressed states. *Phys. Rev. Lett.* **116**, 230503 (2016).
43. Zhou, B. B. et al. Accelerated quantum control using superadiabatic dynamics in a solid-state lambda system. *Nat. Phys.* **13**, 330–334 (2017).
44. Cirac, J. I., Zoller, P., Kimble, H. J. & Mabuchi, H. Quantum state transfer and entanglement distribution among distant nodes in a quantum network. *Phys. Rev. Lett.* **78**, 3221–3224 (1997).
45. Korotkov, A. N. Flying microwave qubits with nearly perfect transfer efficiency. *Phys. Rev. B* **84**, 014510 (2011).
46. Sete, E. A., Mlinar, E. & Korotkov, A. N. Robust quantum state transfer using tunable couplers. *Phys. Rev. B* **91**, 144509 (2015).
47. Yin, Y. et al. Catch and release of microwave photon states. *Phys. Rev. Lett.* **110**, 107001 (2013).
48. Wenner, J. et al. Catching time-reversed microwave coherent state photons with 99.4% absorption efficiency. *Phys. Rev. Lett.* **112**, 210501 (2014).
49. Srinivasan, S. J. et al. Time-reversal symmetrization of spontaneous emission for quantum state transfer. *Phys. Rev. A* **89**, 033857 (2014).
50. Pechal, M. et al. Microwave-controlled generation of shaped single photons in circuit quantum electrodynamics. *Phys. Rev. X* **4**, 041010 (2014).
51. Zeytinoglu, S. et al. Microwave-induced amplitude- and phase-tunable qubit-resonator coupling in circuit quantum electrodynamics. *Phys. Rev. A* **91**, 043846 (2015).
52. Xiang, Z. L., Zhang, M., Jiang, L. & Rabl, P. Intracavity quantum communication via thermal microwave networks. *Phys. Rev. X* **7**, 011035 (2017).
53. Vermersch, B., Guimond, P.-O., Pichler, H. & Zoller, P. Quantum state transfer via noisy photonic and phononic waveguides. *Phys. Rev. Lett.* **118**, 133601 (2017).
54. Steffen, M. et al. Measurement of the entanglement of two superconducting qubits via state tomography. *Science* **313**, 1423–1425 (2006).
55. Neeley, M. et al. Process tomography of quantum memory in a Josephson-phase qubit coupled to a two-level state. *Nat. Phys.* **4**, 523–526 (2008).

Acknowledgements We thank P. J. Duda, A. Clerk and K. J. Satzinger for discussions. We thank W. D. Oliver and G. Calusine at MIT Lincoln Lab for providing the travelling-wave parametric amplifier (TWPA) used in this work. Devices and experiments were supported by the Air Force Office of Scientific Research and the Army Research Laboratory. É.D. was supported by LDRD funds from Argonne National Laboratory; A.N.C. was supported in part by the DOE, Office of Basic Energy Sciences, and D.I.S. acknowledges support from the David and Lucile Packard Foundation. This work was partially supported by the University of Chicago’s MRSEC (NSF award DMR-2011854) and made use of the Pritzker Nanofabrication Facility, which receives support from SHyNE, a node of the National Science Foundation’s National Nanotechnology Coordinated Infrastructure (NSF grant number NNC1542205), with additional support from NSF QLCI for HQAN (NSF award 2016136).

Author contributions Y.Z. designed and fabricated the devices, performed the measurement and analysed the data. H.-S.C. provided help with the measurement. A.B. and É.D. provided help with the infrastructure setup. A.N.C. and D.I.S. advised on all efforts. All authors contributed to discussions and production of the manuscript.

Competing interests The authors declare no competing interests.

Additional information

Supplementary information The online version contains supplementary material available at <https://doi.org/10.1038/s41586-021-03288-7>.

Correspondence and requests for materials should be addressed to A.N.C.

Peer review information *Nature* thanks Damian Markham and the other, anonymous, reviewer(s) for their contribution to the peer review of this work.

Reprints and permissions information is available at <http://www.nature.com/reprints>.